Triangular Si_3N_4 nano-scale pits on the stepped Si (553) surface by ion induced reaction

Amit Kumar Singh Chauhan[1,2], Shibin Krishna T.C.[1], Neha Aggarwal[1], Monu Mishra[1], Asad Niazi[2], Lekha Nair[2], Govind Gupta[1*]

[1]*Physics of Energy Harvesting, National Physical Laboratory (CSIR-NPL), Dr. K.S. Krishnan Road, New Delhi 110012, India*
[2]*Department of Physics, Jamia Millia Islamia, New Delhi 110025, India*

[*]Corresponding author. Tel: (+91) 11-45608403; E-mail: govind@nplindia.org

ABSTRACT

Triangular nano-scale pits (TNPs) of Si_3N_4 are fabricated by reactive nitrogen ion sputtering using low energy nitrogen ions on the Si (553) surface at 500 °C. The electronic structure of the developing Si_3N_4 interface was monitored in-situ by Auger Electron Spectroscopy (AES) while the ion beam induced surface reaction was analysed via X-Ray and Ultraviolet photoemission spectroscopy (XPS & UPS), Photoluminescence and Raman spectroscopy. The morphological development of nanoscale pit structures was observed by Scanning Electron Microscopy (SEM). The formation of Si_3N_4 was identified by AES, with the appearance of the characteristic reacted Si(LVV) peak at 83 eV, while photoemission spectroscopy confirmed the stoichiometry of Si_3N_4. The valence band maximum was observed to be located at 2.4 eV below the Fermi level. SEM images showed uniformly distributed Si_3N_4 TNPs with size varying between 250 to 600 nm (length) and 200 to 400 nm (width). Our work underlines the influence of ion energy and substrate temperature and establishes the conditions for the growth of Si_3N_3 TNPs by ion induced reactive sputtering. Copyright © 2015 VBRI Press.

Keywords: Triangular nanostructures; Si_3N_4; AES; XPS; SEM.

Introduction

Recently, the heteroepitaxial growth of III-nitrides structures on silicon (Si) has attracted considerable attention as a substitute for sapphire in the development of nitride based devices like high electron mobility transistors (HEMTs) and light emitting diodes (LEDs) [1-3]. To reduce the dislocation density in films grown on Si substrates, the growth of an intermediate Si_xN_y layer is proposed. It would act as a stress sink, inhibiting dislocation formation and facilitating the growth of high quality III-N films and their nanostructures [4-7]. Recent reports indicate that nanostructured Si_xN_y templates have been used for the growth of III-N nanostructures, where the patterned template assists efficient dislocation filtering [8-10]. A number of techniques have been employed to develop patterned or nanostructured Si_xN_y templates, such as focused ion beam milling, reactive ion implantation and lithography for selective area growth, followed by metal organic vapour phase epitaxy and molecular beam epitaxy for self-assembled nanostructure growth [9-12].

In the present study, reactive ion sputtering by low energy nitrogen (N_2^+) ions has been utilised to form well-ordered and spatially distributed Si_xN_y nano-scale pits on the high index stepped Si (553) surface.
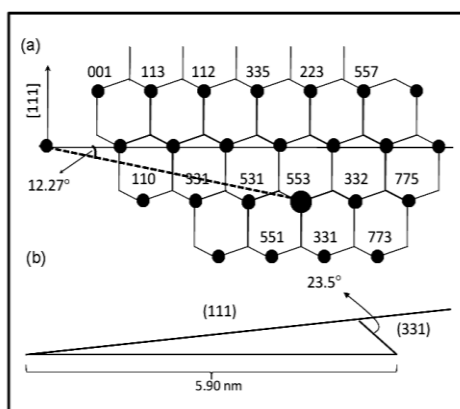
Ion beam induced surface nano patterning has been studied in recent times as an interesting phenomenon of fundamental interest, as well as an increasingly wide range of applications [13, 14]. Sputtering of semiconductor surfaces in the low keV range leads to the self organised development of ripples and dot patterns which echo windblown patterns on sand, while ion irradiation of metal films on crystalline substrates (with energy in the several 10's of keV to the MeV region) has resulted in the development of nanostructures with narrow size distributions due to sputtering or thermal spike driven dewetting [15-17]. Glancing incidence irradiation of insulators has resulted in the development of well-spaced nanodots and selective depletion of certain species along the ion track [18, 19]. The low energy ion sputtering technique offers a number of advantages such as availability of laboratory ion sources, selection of the incident ion energy and direction, simplicity of focusing, absence of undesirable impurities and the ability to form nanostructures on the surface by altering the chemical nature of the materials in the desired direction [20]. Nano-patterning by ion sputtering may also be governed by substrate parameters such as target temperature [21] and initial surface crystal structure & orientation [22-25].

Recently, the growth of Si_xN_y thin film was reported on planar Si (111)/(100)/(400) surfaces where nitrogen plasma was used for the nitridation of the surface [26, 27]. The Si_3N_4 lattice is well matched with the III-Nitride materials, forming a thin layer (~1.5 nm), which acts as diffusion barrier and blocks the inter diffusion of group III elements

(Ga, Al, In etc.) into the substrate. Si_3N_4 possess high strength at high temperatures, good resistance to oxidation as well as low coefficient of thermal expansion which offers good thermal stress resistance [28]. This material is also widely used in energy conversion devices [28]. Recent studies reported that pits on Si surface exhibits different energetics, increase in stress/strain, high conductivity and ultimately promote the nucleation [29]. Hence, further deposition of material may become more localised inside these pits which may assist the growth of aligned nanostructures. These surface pits with different energetics and properties can also be used for various nanoelectronic and optoelectronic devices [30, 31].

In our experiments, ion irradiation was carried out on the Si sample at room temperature (RT) as well as at high temperature (500 ^{o}C) and with increasing ion energies, while the reactivity is monitored by AES, XPS and UPS. The Si (553) surface was chosen to grow Si_3N_4 TNPs as it is a stepped surface with greater dangling bond density than the low index surfaces, which should promote reactivity with the incident ions. The Si (553) is tilted at -12.27° from the (111) planes as shown in **Fig**. 1(**a**), which presents a cross-sectional schematic view of bulk Si. The unit cell of the (553) surface is comprised of one unit each of the (111) (7x7 or 5x5) and (331) (1x1) facet (shown in **Fig**. **1** (**b**)), which results in a shallow hill & valley like morphology [32]. The surface structure of Si (553) could bias momentum transfer from the incident ions in certain directions and support the formation of aligned Si_xN_y nanostructures.

Fig. 1. (a) Cross-sectional view of the bulk Si showing the Si(553) surface which lies -12.27° from the (111) plane and (b) Schematic drawing of the Si (553) surface, which shows an alternating arrangement of (111) and (331) facets with angle 23.5° between them.

The present manuscript is organised as follows: after the introduction, the experimental procedure and techniques are discussed in section 2. Significant experimental results using various characterisation techniques and the possible mechanisms for the ion induced reaction and development of TNPs are presented and discussed in section 3. The conclusions are summarised in section 4.

Experimental

The surface preparation and irradiation were carried out in an ultra-high vacuum (UHV) system equipped with Auger electron spectroscopy (AES), reverse view low energy electron diffraction (Er-LEED) and a sputter ion gun, operating at a base pressure of $5x10^{-11}$ Torr. The samples were mounted on a high precision 4-axis manipulator that enabled their positioning for growth and analysis. Samples of size 20 x 8 x 0.35 mm^3 were cut from a p-type (Boron doped) Si (553) wafer having a resistivity of 10-20 Ω cm. The samples were first cleaned in ambient conditions by the modified Shiraki process [33] and then transferred to the UHV system and prepared in-situ by annealing at 600 °C for ~ 6 hours, before flashing at 1100 °C for 5 seconds, followed by slow cooling to RT. The cleanliness of the sample was ascertained by AES. A W-Re (5% - 25%) thermocouple was attached to the sample for precise temperature measurement.

N_2^+ ions from the sputter ion gun (Perkin Elmer PHI-04-300) at normal incidence were used for the nitridation of Si (553) surface. The 5N (99.999 % pure) nitrogen gas was filled in the collision chamber (discharge tube) of the ion gun through a needle valve, to control the pressure within the tube. The voltage was kept at the desired value and typical ion current between 1.8 and 2 μA was used. The pressure in the UHV chamber was kept to $\sim1x10^{-7}$ torr during irradiation. After ion irradiation (and cooling the samples to RT in the case of the high temperature (HT) samples) AES spectra were recorded. The X-Ray and Ultraviolet photoelectron spectroscopy (XPS & UPS) measurements were carried out in an OMICRON Multi-probe Surface Analysis System operating at a base pressure of 5×10^{-11} Torr. MgK_α (1253.6 eV) and He-I (21.2 eV) radiation was employed for XPS and UPS measurements respectively. The calibration of binding energy in the photoemission spectra was carried out with reference to standard gold samples, with the Au $4f_{7/2}$ emission line used for XPS and the Au Fermi level for UPS [34]. The core level (CL) fitting has been done using Shirley background subtraction and Gaussian line shape, after the necessary carbon correction. The scanning electron microscopy (SEM) images have been recorded using a JEOLJSM-6700F field-emission scanning electron microscope (FESEM, operating at 15 kV). Steady state fluorescence spectroscopy was carried out using a Fluorolog (Jobin Yvon-Horiba, model-3-11) spectro-fluorometer and Micro-Raman measurements were performed at RT using a Triple Raman Spectrometer in the backscattering configuration, where an Argon ion laser (Ar$^+$) operating at a wavelength of 514 nm with a maximum power of 50 mW was used as the excitation source.

Results and discussion

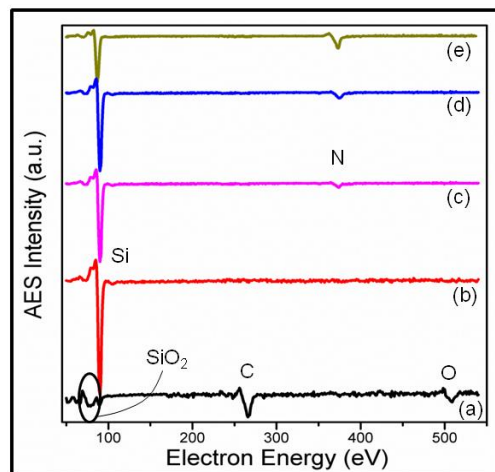*Chemical / structural properties of Si_3N_4 sample AES analysis*

Prior to irradiation, the samples were cleaned ex-situ as described earlier and then introduced into the UHV chamber and characterised by AES to evaluate the elemental and chemical composition of the sample surface. The evaluation was repeated at various stages of the experiment to track the changes in chemical composition. The AES survey scans of the 'as loaded', UHV cleaned and irradiated Si samples are shown in **Fig. 2** (curves a-e) where the AES signal intensity is plotted as a function of Auger electron kinetic energy. Curve (a) shows the survey

scan of the 'as loaded' sample before flashing at 1100 °C, where the presence of peaks at 92 eV, 272 eV & 511 eV corresponding to the characteristic Auger transitions of Si (LVV), C (KLL) and O (KLL) respectively were observed. The occurrence of the 'oxidised Si' peak at 76 eV indicates the presence of native oxides as a passivation layer of SiO_2 on the Si (553) surface. After flashing the sample at 1100 °C, the atomically clean Si (553) surface was attained, as confirmed by the presence of an intense and sharp Si(LVV) Auger transition at 92 eV (curve (b)) and the disappearance of the C and O signal below the AES detection limit. The atomically clean Si (553) surface has been used for the fabrication of Si_xN_y at RT and HT, via ion bombardment using N_2^+ ions for 60 minutes at two different values of ion energy (500 eV and 2.0 keV). Curve (c) shows the AES spectra for the sample at RT following irradiation by 500 eV N_2^+ ions. In this curve, a large peak at 90 eV and small peak at 378 eV were observed which correspond to the Si (LVV) and N (KLL) Auger transitions respectively. The presence of the N species on the Si (553) surface and a chemical shift (2 eV) in the Si peak position towards lower kinetic energy indicates the reaction between Si and N atoms. The Auger intensity ratio of N (KLL) and Si (LVV) peak intensity ($I_{N/Si}$) was found to be 0.063. Since the substrate temperature is an important factor for ion induced surface modification [**35**], the preparation of Si_xN_y was also carried out at elevated temperature. Curve (d) displays the AES spectra for the Si_xN_y sample fabricated at a substrate temperature of 500 °C during irradiation by 500 eV ions. The Si (LVV) and N (KLL) Auger transitions were observed at 86 eV and 378 eV respectively. The AES signal intensity of N (KLL) peak was observed to be higher than that of the RT grown sample. The Si peak also showed a chemical shift of 6 eV from the clean Si value of 92 eV. The value of $I_{N/Si}$ for the sample surface was found to be 0.089. The increment in the N peak intensity was a consequence of enhanced surface reactivity due to the higher substrate temperature (500 °C).

Further enhancement in surface reactivity was observed for the sample irradiated by higher N_2^+ ion energy (2 keV) (curve (e)). The N (KLL) peak intensity increased significantly when 2 keV N_2^+ ions at 500 °C were used for Si_xN_y formation, where the value of $I_{N/Si}$ is found to be 0.333. The significant enhancement in $I_{N/Si}$ value was ascribed to the higher contribution of N and reduction in the Si peak due to the attenuation of the Si signal by the presence of more energetic N species on the surface. Furthermore, the peak position of Si (LVV) was shifted to 83 eV which corresponds to the characteristic AES peak position of Si_3N_4 [**36**].
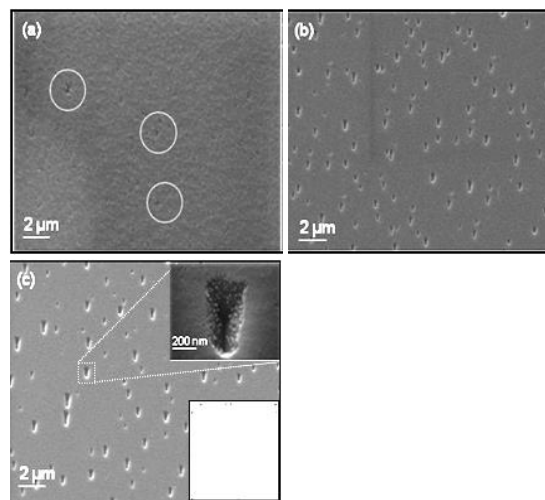
The conversion of Si to Si_xN_y is attributed to the enhanced surface reactivity resulting from the higher energy of N_2^+ ions at 2 keV. This energy is almost five times higher than the energy threshold for ion induced surface reactions with nitrogen atoms on silicon, which has an impact on the reactivity as explained in the discussion section. The AES analysis revealed that optimal conditions for the formation of fully reacted Si_3N_4 occur upon irradiation with 2 keV N_2^+ ions by keeping the sample at 500 °C, and the subsequent studies emphasise the analysis of these TNPs.

Fig. 2. AES survey spectra of (a) as loaded Si (553) sample, (b) atomically cleaned Si (553) surface. SiN samples using N^{2+} ions (c) 500 eV at RT, (d) 500 eV at 500 °C,(e) 2 keV at 500 °C.

SEM analysis

The surface morphology of the surfaces which showed beam induced reactivity was examined by SEM measurements. **Fig. 3**(**a**) shows the surface morphology of the RT grown sample, where the surface is found to be covered with small pit like structures.
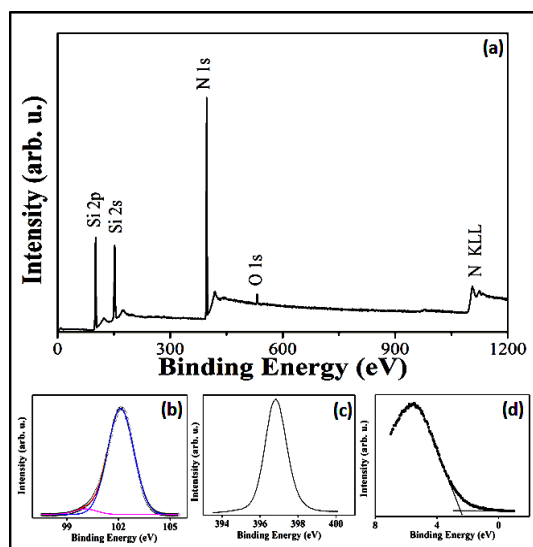

Fig. 3. SEM image of as-grown Si_3N_4 (a) at RT, 500 eV (pits are shown in circles), (b) 500 °C with 500 eV N_2^+ ions and (c) 500 °C with 2 keV N_2^+ ions (Inset shows the zoomed SEM micrograph of an individual triangular nanostructure of Si_3N_4).

Fig. 3(**b**) shows the SEM micrograph for the sample grown at 500 °C with 500 eV N_2^+ ion energy, where the surface was covered with small & large triangular shaped Si_xN_y pits with size varying from 150 to 300 nm (length) and 70 to 180 nm (width). The average density of these triangular nano-scale pits (TNPs) was observed to be ~8 x 10^8 cm^{-2}. The SEM micrograph for the Si_xN_y sample grown at 500 °C using 2 keV N_2^+ ions is shown in **Fig. 3** (**c**). The surface has shows the development of uniformly large TNPs, with size varying between 250 to 600 nm (length) and 200 to 400 nm (width). The average density of these TNPs is found to be ~2x10^8 cm^{-2}. The upper inset of **Fig. 3**(**c**) shows the magnified micrograph of a single TNP. The

size of this particular TNP is observed to be 600 nm (length) and 350 nm (base width). The lower inset illustrates the schematic representation of the observed single triangular Si_xN_y pit indicating the large surface area associated with these nano-scale pits. The size variation in the SEM images revealed that both ion energy and substrate temperature strongly influence the development of these Si_xN_y nanostructures.

XPS and UPS characterisation

To characterise the extent of chemical bonding between Si and N, XPS & UPS analysis of the completely formed TNP Si_xN_y surface (500 ^{o}C, 2 keV N_2^+ ions) were performed. **Fig. 4(a)** shows the XPS survey scan of Si_xN_y -TNPs while Si(2p) and N(1s) core level spectra are shown in **Fig. 4(b)** and (**c**) respectively.

Fig. 4. XPS (a) Survey scan and core level spectra of (b) Si (2p) and (c) N (1s) of Si_3N_4-TNPS and (d) UPS Valence Band spectra.

The survey scan (**Fig. 4(a)**) shows the presence of Si(2p), Si(2s), N(1s), O(1s) core level peaks and N(KLL) Auger lines at their respective binding energy positions [**37**]. The stoichiometry of the film was estimated from the XPS survey scan using the following equation:
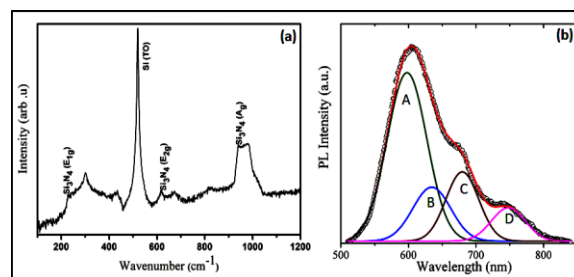
$$Si : N = I_{Si/N} \times \frac{A_N}{A_{Si}}$$

(1)

where, $I_{(Si/N)}$ is the intensity ratio of Si(2p) and N(1s) core level spectra while A_{Si} and A_N are their respective atomic sensitivity factors (ASF) [**37**]. The ASF for Si(2p) and N(1s) were 0.27 and 0.42, and accordingly the obtained value of Si:N was found to be 0.73 (~3/4), confirming the formation of Si_3N_4 on the surface. The Si(2p) XPS core level spectrum (**Fig. 4(b)**) was de-convoluted into two identified peaks centred at 99.8 eV and 102.2 eV, which are assigned to Si-Si (5%) and Si-N (95%) bonds respectively [**38, 39**]. The N(1s) core level peak (**Fig.4(c)**) was located at 396.9 eV and assigned to Si_3N_4 [**35**].

The valence band structure of Si_3N_4-TNPs was examined by UPS valence band (VB) spectrum obtained via using He(I) radiation (21.2 eV) and is shown in **Fig.**

4(d). The position of the VB maximum was calculated by extrapolating a linear fit to the leading edge of the VB photoemission to the baseline. The VB maximum position is calculated to be 2.4 eV, which is found to be in accord with recently reported values [**40, 41**].

Raman and photoluminescence analysis

Fig. 5 (**a**) shows the linear plot of the room temperature Raman spectra obtained from the Si_3N_4 TNPs (500 ^{o}C and 2 keV N_2^+ ions) film. A sharp peak of bulk Si achieved at 520 cm^{-1} relates to the Transverse Optical (TO) mode in crystalline-Si. Raman bands in the region 600-1100 cm^{-1} can be associated with the stress dependency. Bands of Si_3N_4 near 230, 620 and 940 cm^{-1} corresponds to E_{1g}, E_{2g} and A_g modes respectively [**42**]. In our case, bands associated with these modes are obtained with a shift, at 226, 618 and 940 cm^{-1} respectively. Further, the nano-patterned Si_3N_4 film grown on the Si (553) substrate exhibits strong visible photoluminescence (PL) when excited at radiation of 450 nm in the RT.
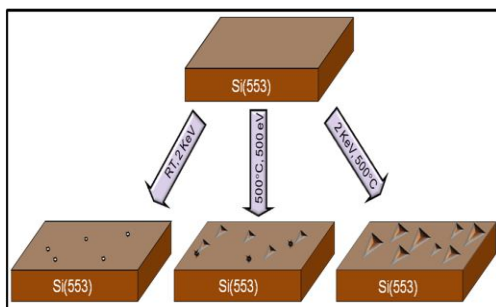

Fig. 5. (a) RT- Micro Raman spectra and (b) deconvoluted RT-PL spectra of TNPs-Si_3N_4 film grown on Si (553) substrate.

Fig. 5 (**b**) shows the de-convoluted PL spectra of the Si_3N_4 TNPs (500 ^{o}C and 2 keV N_2^+ ions), which illustrates a strong PL emission in the visible region with a maximum intensity at 604 nm, although the observed broad peak has multiple peaks convoluted together. A detailed, self-consistent, simultaneous fit was carried out which indicates the presence of four components, A, B, C, D, convoluted within the broad envelope situated at 596 nm, 638 nm, 685 nm and 747 nm, respectively. Robertson [**43**] and Mohammed *et. al.* [**44**] has introduced models to understand the origin of these multiple PL emission peaks in Si_3N_4 films. On the basis of these models, the following transitions between the band edges and the defect states can be correlated with the observed PL peak intensities: Peak A (596 nm, 2.08 eV) was assigned to a transition from the host conduction band to the negatively charged Si dangling bond state ($E_C \rightarrow Si^-$) with equivalent contribution from negatively charged Si dangling bond state to the N dangling bond state ($Si^- \rightarrow N^-$). Peak B (638 nm, 1.95 eV) was attributed to the positively charged Si dangling bond state to the N dangling bond state ($Si^+ \rightarrow N^-$) transition. These two transitions are mainly associated with the Si dangling bond to N dangling bond states of TNPs Si_3N_4 matrix. Peak C (685 nm, 1.81 eV) and D (747 nm, 1.66 eV) corresponds to the transitions from negatively and positively charged Si dangling bond states to the valence band edge, i.e. $Si^- \rightarrow E_V$ & $Si^+ \rightarrow E_V$, respectively [**44**]. The contribution of the peak A and B is larger among the convoluted peaks, which

implies that the PL spectra of Si_3N_4 TNPs originates mainly from Si and N dangling bond states present within the material, and not due to quantum confinement.

Mechanism of reaction and growth

When an energetic ion bombards on a surface, it transfers energy to the atoms of the target and eventually comes to rest. The energy loss process is typically classified into two types: nuclear and electronic energy loss [45]. At low incident energy, typically in the few keV regimes, there is a momentum transfer through Rutherford type nuclear collisions resulting in sputtering or local atom displacement. As the velocity of the incident atom approaches the Bohr velocity of the electrons in the target, electronic energy loss occurs, i.e., the ion can transfer energy to the electrons in the target, resulting in interband transitions, electron-hole pair production and ionisation [46].

Fig. 6. Schematic diagram for the growth of TNPs-Si_3N_4 on Si (553) substrate.

Funsten *et al.* [47] has determined ion energy thresholds for e-h pair production in silicon for several sets of incident ions. N_2^+ ions of 500 eV have velocity 35% above this threshold, which results in some reactivity even at room temperature. At higher incident energy, reactivity is enhanced further since more of the conduction band density of states becomes accessible at this energy [48]. Elevated sample temperature also enhances atom mobility on the surface and facilitates reactive etching. Thus, the formation of triangular shaped Si_3N_4 nano-scale pits on Si (553) is enhanced by both increased energy and temperature. For the substrate at RT, the interaction of energetic N_2^+ ions with Si atoms of the surface caused some reaction at the surface, but in case of high substrate temperature, the temperature induced mobility of surface Si atoms enhances reactivity and facilitates sputtering [22]. For Si_3N_4 TNPs formed on the Si (553) surface at 500 ^{o}C with 500 eV and 2 keV N_2^+ ion energies the surface morphology (size and uniformity) changes with increase in the ion energy. Upon increasing the ion energy from 500 eV, nearby small individual blisters begin to coalesce and as energy is increased further, the coalescence proceeds progressively as a result of which blister size increases. While their areal density decreases, as indicated in the schematic of **Fig. 6**. Increase in ion energy beyond 2 keV leads to a large amount of sputtering of the surface resulting in the formation of craters (not shown here).

In addition to the substrate temperature and ion beam energy for the creation of Si_3N_4 TNPs, surface morphology

of the substrate also plays an important role [24]. The unique surface morphology of the Si (553) surface, consisting of hill and valley structures (as shown in **Fig. 1** (**b**)), supports the formation of Si_3N_4 TNPs. The hill and valley surface structures act as localised perturbations for collision cascades, which enable more energy from the collision cascades to reach the valleys rather than the hills. This manifests as preferential sputtering of the valleys [49]. The instability along with thermal diffusion and the post growth cooling to RT results in the formation of these TNPs. Thus, the effect of substrate temperature, energy of the N_2^+ ions and the surface morphology of the substrate are the presiding factors for ion induced formation of triangular Si_3N_4 nanostructures on high index Si (553) surface. The direction oriented Si_3N_4 TNPs could be potentially employed in the selective area growth of aligned III-Nitride nanostructures.

Conclusion

We have demonstrated the formation of triangular shaped Si_3N_4 nano-scale pits via ion induced surface reactivity and structural transformation, on a stepped Si (553) surface at 500 °C by N_2^+ ions of 500 eV and 2 keV energy. *In-situ* AES analysis confirmed the formation of Si_3N_4 which showed the characteristic AES peak of Si (Si_3N_4) at 83 eV. The SEM characterisation revealed that the size of the TNPs vary between 250 to 600 nm in length and 200 to 400 nm in width with an average density of ~5x 10^8 cm^{-2} on the surface. The substrate temperature and ion beam energy played a significant role in the formation of these triangular pits on Si (553) surface, apart from the surface morphology of this substrate, which also provides favourable conditions for the formation of the TNPs. This study will help to understand the mechanism involved at the interface during the ion induced surface modification and their dependence on ion energy, incidence geometry and substrate temperature for the growth of Si_3N_4 on high index Si surfaces. These TNP-Si_3N_4 surfaces can be exploited as potential substrates for controlled and selective area growth of III-nitride nanostructures.

Author contributions

Conceived the plan AKSC, GG:; Performed the expeirments: AKSC, SKTC, NA, MM , GG ; Data analysis: AKSC, SKTC, NA, MM, LN, GG; Wrote the paper: AKSC, AN, LN, GG. Authors have no competing financial interests.

Reference

1. Radhakrishnan, K.; Dharmarasu, N.; Sun, Z.; Arulkumaran, S.; Ng, G.I.; *Appl. Phys. Lett.*, **2010**, *97*, 232107.
    DOI: 10.1063/1.3518717
2. Tripathy, S.; Lin, V.K.X.; Dolmanan, S.B.; Tan, J.P.Y.; Kajen, R.S.; Bera, L.K.; Teo, S.L.; Kumar, M.K.; Arulkumaran, S.; Ng, G.I.; Vicknesh, S.; Todd, S.; Wang, W.Z.; Lo, G.Q.; Li, H.; Lee, D.; Han, S.; *Appl. Phys. Lett.*, **2012**, *101*, 082110.
    DOI: 10.1063/1.4746751
3. Liu, J.; Feng, F.; Zhou, Y.; Zhang, J.; Jiang, F.; *Appl. Phys. Lett.*, **2011**, *99*, 111112.
    DOI: 10.1063/1.3640229

4. Dadgar, A.; Hums, C.; Diez, A.; Blasing, J.; Krost, A.; *J. Cryst. Grow.*, **2006**, *297*, 279.
   DOI: 10.1016/j.jcrysgro.2006.09.032
5. Yamabe, N.; Shimomura, H.; Shimomura, T.; Ohachi, T.; *J. Crys. Grow.*, **2009**, *311*, 3049.
   DOI: 10.1016/j.jcrysgro.2009.01.076
6. Zang, K.Y.; Wang, Y.D.; Wang, L.S.; Chow, S.Y.; Chua, S.J.; *J. Appl. Phys.*, **2007**, *101*, 093502.
   DOI: 10.1063/1.2724793
7. Dadgar, A.; Poschenrieder, M.; Reiher, A.; Blasing, J.; Christen, J.; Krtschil, A.; Finger, T.; Hempel, T.; Diez, A.; Krost, A.; *Appl. Phys. Lett.*, **2003**, *82*, 28.
   DOI: 10.1063/1.1534940
8. Zubia, D.; Herse, S.D.; *J. Appl. Phys.*, **1999**, *85*, 6492.
   DOI: 10.1063/1.370153
9. Colby, R.; Liang, Z.; Wildeson, I.H.; Ewoldt, D.A.; Sands, T.D.; Garcia, R.E.; Stach, E.A.; *Nano Lett.*, **2010**, *10*, 1568.
   DOI: 10.1021/nl9037455
10. Wildeson, I.H.; Ewoldt, D.A.; Colby, R.; Stach, E.A.; Sands, T.D.; *Nano Lett.*, **2011**, *11*, 535.
    DOI: 10.1021/nl103418q
11. Liu, C.; Wang, W.N.; Denchitcharoen, S.; Gott, A.; Shields, P.A.; Allsopp, D.W.E.; *Phys. Stat. Sol. C*, **2009**, *6*, S527.
    DOI: 10.1002/pssc.200880801
12. Kumar, P.; Kumar, M.; Govind; Mehta, B.R.; Shivaprasad, S.M.; *MRS Proceedings*, **2009**, *1202*, 1202-I05-09.
    DOI: 10.1557/PROC-1202-I05-09
13. Garcia, J.M.; Vazquez, L.; Cuerno, R.; Garcia, J.A.S.; Castro, M.; Gago, R. Self-organized Surface Nanopatterning by Ion Beam Sputtering, In Toward Functional Nanomaterials; Wang, Z.M. (Ed.); Springer: *New York*, **2009**, 323.
    DOI: 10.1007/978-0-387-77717-7_10
14. Chauhan, A.K.S.; Kumar, M.; Gupta, G.; *Appl. Surf. Sci.*, **2015**, *345*, 156.
    DOI: 10.1016/j.apsusc.2015.03.167
15. Facsko, S.; Dekorsy, T.; Koerdt, C.; Trappe, C.; Kurz, H., Vogt, A., Hartnagel, H.L., *Science*, **1999**, *285*, 1551.
    DOI: 10.1126/science.285.5433.1551
16. Attri, A.; Asokan, K.; Nair, L.; *Adv. Sci. Lett.*, **2014**, *20*, 1446.
    DOI: 10.1166/asl.2014.5510
17. Attri, A.; Kumar, A.; Verma, S.; Ojha, S.; Asokan, K.; Nair, L.; *Nanoscale Res. Lett.*, **2013**, *8*, 433.
    DOI: 10.1186/1556-276X-8-433
18. Akcoltekin, E.; Peters, T.; Meyer, R.; Duvenbeck, A.; Klusmann, M.; Monnet, I.; Lebius, H.; Schleberger, M.; *Nature Nanotech.*, **2007**, *2*, 209.
    DOI: 10.1038/nnano.2007.27
19. Ochedowski, O.; Osmani, O.; Schade, M.; Bussmann, B.K.; Band'Etat, B; Lebius, H.; Schleberger, M.; *Nature Comm.*, **2014**, *5*, 3913.
    DOI: 10.1038/ncomms4913
20. Kawabata, T.; Okuyama, F.; Tanemura, M.; *J. Appl. Phys.*, **1991**, *69*, 3723.
    DOI: 10.1063/1.348465
21. Madi, C.S.; George, H.B.; Aziz, M.J.; *J. Phys.: Cond. Mat.*, **2009**, *21*, 224010.
    DOI: 10.1088/0953-8984/21/22/224010
22. Ziberi, B.; Cornejo, M.; Frost, F.; Rauschenbach, B.; *J. Phys.: Cond. Mat.*, **2009**, *21*, 224003.
    DOI: 10.1088/0953-8984/21/22/224003
23. Valbusa, U.; Boragno, C.; Mongeot, F.B.D.; *J. Phys.: Cond. Mat.*, **2002**, *14*, 8153.
    DOI: 10.1088/0953-8984/14/35/301
24. Cuerno, R.; Barabasi, A.L.; *Phys. Rev. Lett.*, **1995**, *74*, 4746.
    DOI: 10.1103/PhysRevLett.74.4746
25. Otto, G.; Hobler, G.; Palmetshofer, L.; Mayerhofer, K.; Piplits, K.; Hutter, H.; *Nucl. Instrum. Methods in Phys. Res. B*, **2006**, *242*, 667.
    DOI: 10.1016/j.nimb.2005.08.140
26. Bahari, A.; Robenhagen, U.; Morgen, P.; Li, Z.S.; *Phys. Rev. B*, **2005**, *72*, 205323.
    DOI: 10.1103/PhysRevB.72.205323
27. Dorranian, D.; Azadfar, P.; Sari, A.H.; Ghorbani, S.; Hojabri, A.; Ghoranneviss, M.; *Eur. Phys. J. Appl. Phys.*, **2008**, *42*, 103.
    DOI: 10.1051/epjap:2008039
28. Ziegler, G.; Heinrich J.; Wotting, G.; *J. Mater. Sci.*, **1987**, *22*, 3041.
    DOI: 10.1007/BF01161167
29. Verveniots, E.; Rezek, B.; Sipek, E.; Stuchlik, J.; Ledinsky M.; Kocka, J.; *Nanoscale Res. Lett.*, **2011**, *6*, 145.
    DOI: 10.1186/1556-276X-6-145
30. Wang, H.; Zhang, Z.; Wong, L.M.; Wang, S.; Wei, Z.; Li, G.P.; Xing, G.; Guo, D.; Wang D.; Wu, T.; *ACS Nano*, **2010**, *4*, 2901.
    DOI: 10.1021/nn1000996
31. Wang, H.; Wo, T.; *Nanoscale Res. Lett.*, **2012**, *7*, 110.
    DOI: 10.1186/1556-276X-7-110
32. Hara, S.; Yoshimura, M.; Ueda, K.; *Jpn. J. Appl. Phys.*, **2008**, *47*, 6102.
    DOI: 10.1143/JJAP.47.6102
33. Enta, Y.; Suzuki, S.; Kono, S.; Sakamoto, T.; *Phys. Rev. B*, **1989**, *39*, 5524.
    DOI: 10.1103/PhysRevB.39.5524
34. Hong, S.K.; Hanada, T.; Makino, H.; Chen, Y.; Ko, H.J.; Yao, T.; Tanaka, A.; Sasaki, H.; Sato, S.; *Appl. Phys. Lett.*, **2001**, *78*, 3349.
    DOI: 10.1063/1.1372339
35. Bhattacharjee, S.; Karmakar, P.; Chakrabarti, A.; *Nucl. Instr. Meth. Phys. Res. B: Beam Inter. with Mat. & Atoms*, **2012**, *278*, 58.
    DOI: 10.1016/j.nimb.2012.02.004
36. Bermudez, V.M.; Perkins, F.K.; *Appl. Surf. Sci.*, **2004**, *235*, 406.
    DOI: 10.1016/j.apsusc.2004.02.065
37. Wagner, C.D.; Riggs, W.M.; Davis, L.E.; Moulder, J.F.; Muilenberg, G.E.; Handbook of X-Ray Photoelectron Spectroscopy; Perkin Elmer Corp.: USA, 1981.
38. Ravizza, E.; Spadoni, S.; Piagge, R.; Comite, P.; Wieme, C.; *Surf. Inter. Ana.*, **2012**, *44*, 1209.
    DOI: 10.1002/sia.4943
39. Nguyen, A.T.; Baggerman, J.; Paulusse, J.M.J.; van-Rijn, C.J.M.; Zuilhof, H.; *Langmuir*, **2011**, *27*, 2587.
    DOI: 10.1021/la104657c
40. Cook Jr., T.E.; Fulton, C.C.; Mecouch, W.J.; Davis, R.F.; Lucovsky, G.; Nemanich, R.J.; *J. App. Phy.*, **2003**, *94*, 3949.
    DOI: 10.1063/1.1601314
41. Yang, M.; Chai, J.W.; Wang, Y.Z.; Wang, S.J.; Feng, Y.P.; *J. Phys. Chem. C*, **2012**, *116*, 22315.
    DOI: 10.1021/jp304054u
42. Honda, K.; Yokoyama, S.; Tanaka, S.; *J. Appl. Phys.*, **1999**, *85*, 7380.
    DOI: 10.1063/1.369366
43. Robertson, J.; *Philos. Mag. B*, **1991**, *63*, 47.
    DOI: 10.1080/01418639108224430
44. Mohammed, S.; Nimmo, M.T.; Malko, A.V.; Hinkle, C.L.; *J. Vac. Sci. Tech. A*, **2014**, *32*, 021507.
    DOI: 10.1116/1.4861338
45. Avasthi, D.K.; Mehta, G.K.; Swift Heavy Ions for Materials Engineering and Nanostructuring, Springer Series in Materials Science, **2011**, *145*.
    DOI: 10.1007/978-94-007-1229-4
46. Bohr, N.; *Philos. Mag.*, **1913**, *25*, 10,
    DOI: 10.1080/14786440108634305;
47. **1915**, *30*, 581,
    DOI: 10.1080/14786441008635432; *K. Dan. Vidensk. Selsk. Mat. Fys. Medd.*, **1948**, *18*, 8.
48. Funsten, H.O.; Ritzau, S.M.; Harper, R.W.; Borovsky, J.E.; Johnson, R.E.; *Phys. Rev. Lett.*, **2004**, *92*, 213201.
    DOI: 10.1103/PhysRevLett.92.213201
49. Kumar, P.; Nair, L.; Bera, S.; Mehta, B.R.; Shivaprasad, S.M.; *Appl. Surf. Sci.*, **2009**, *255*, 6802.
    DOI: 10.1016/j.apsusc.2009.02.075
50. Bradley, R.M.; Harper, J.M.E.; *J Vac. Sci. Technol. A*, **1988**, *6*, 2390.
    DOI: 10.1116/1.575561